Biomech Model Mechanobiol
DOI 10.1007/s10237-016-0858-2

ORIGINAL PAPER

Verification of a virtual fields method to extract the mechanical properties of human optic nerve head tissues in vivo

Liang Zhang[1,2] · Sri Gowtham Thakku[3] · Meghna R. Beotra[2] · Mani Baskaran[3,4] · Tin Aung[3,5] · James C. H. Goh[6] · Nicholas G. Strouthidis[3,7,8] · Michael J. A. Girard[2,3]

Received: 5 August 2016 / Accepted: 18 November 2016

Abstract We aimed to verify a custom virtual fields method (VFM) to estimate the patient-specific biomechanical properties of human optic nerve head (ONH) tissues, given their full-field deformations induced by intraocular pressure (IOP). To verify the accuracy of VFM, we first generated 'artificial' ONH displacements from predetermined (known) ONH tissue biomechanical properties using finite element analysis. Using such deformations, if we are able to match back the known biomechanical properties, it would indicate that our VFM technique is accurate. The peripapillary sclera was assumed anisotropic hyperelastic, while all other ONH tissues were considered isotropic. The simulated ONH displacements were fed into the VFM algorithm to extract back the biomechanical properties. The robustness of VFM was also tested against rigid body motions and noise added to the simulated displacements. Then, the computational speed of VFM was compared to that of a gold-standard stiffness measurement method (inverse finite element method or IFEM). Finally, as proof of principle, VFM was applied to IOP-induced ONH deformation data (obtained from one subject's eye imaged with OCT), and the biomechanical properties of the prelamina and lamina cribrosa (LC) were extracted. From given ONH displacements, VFM successfully matched back the biomechanical properties of ONH tissues with high accuracy and efficiency. For all parameters, the percentage errors were less than 0.05%. Our method was insensitive to rigid body motions and was also able to recover the material parameters in the presence of noise. VFM was also found 125 times faster than the gold-standard IFEM. Finally, the estimated shear modulus for the prelamina and the LC of the studied subject's eye were 33.7 and 63.5 kPa, respectively. VFM may be capable of measuring the biomechanical properties of ONH tissues with high speed and accuracy. It has potential in identifying patient-specific ONH biomechanical properties in the clinic if combined with optical coherence tomography.

Keywords Ocular biomechanics · Glaucoma · Virtual fields method · Inverse finite element method · Optic nerve head · Intraocular pressure

✉ Michael J. A. Girard
mgirard@nus.edu.sg
http://www.bioeng.nus.edu.sg/OEIL/

1 NUS Graduate School for Integrative Sciences and Engineering, National University of Singapore, Singapore, Singapore

2 Ophthalmic Engineering and Innovation Laboratory, Department of Biomedical Engineering, National University of Singapore, 4 Engineering Drive 3, Block E4 #04-08, Singapore 117583, Singapore

3 Singapore Eye Research Institute, Singapore National Eye Centre, Singapore, Singapore

4 Eye-ACP, Office of Clinical, Academic and Faculty Affairs, Duke-NUS Medical School, Singapore, Singapore

5 Yong Loo Lin School of Medicine, National University of Singapore, Singapore, Singapore

6 Tissue Repair Laboratory, Department of Biomedical Engineering, National University of Singapore, Singapore, Singapore

7 NIHR Biomedical Research Centre, Moorfields Eye Hospital NHS Foundation Trust and UCL Institute of Ophthalmology, London, UK

8 Discipline of Clinical Ophthalmology and Eye Health, University of Sydney, Sydney, NSW, Australia

1 Introduction

Glaucoma is the leading cause of irreversible blindness worldwide (Resnikoff et al. 2004). It is characterized by

Published online: 01 December 2016

the progressive degeneration of retinal ganglion cell (RGC) axons within the optic nerve head (ONH). Within the ONH, RGC axons (Balaratnasingam et al. 2007) pass through the lamina cribrosa (LC), a porous and relatively more compliant connective tissue structure than sclera, before exiting the eye. Excessive deformation of the LC, caused by elevated intraocular pressure (IOP), has been hypothesized as the pathophysiological basis for axonal death (Heijl et al. 2002; Leske et al. 2008; Sommer et al. 1991). However, different susceptibilities of patients to elevated IOP have been observed (Burgoyne et al. 2005; Quigley 2005), suggesting that the biomechanics of the ONH may play a role in glaucoma progression. For instance, biomechanically more compliant tissues may exhibit larger IOP-induced deformations that may lead to axonal damage.

To understand ONH biomechanics, the mechanical properties of this region (comprised of the LC, surrounding peripapillary sclera (PS), choroid, retina and prelaminar tissue) must be determined. In the early days, extraction of human ONH mechanical properties has been limited to linear and nonlinear analyses based on ex vivo experiments, using uniaxial and biaxial testing of tissue strips (Chen et al. 2014; Eilaghi et al. 2010; Friberg and Lace 1988; Geraghty et al. 2012; Graebel and Van Alphen 1977; Schultz et al. 2008; Wollensak and Spoerl 2004). Recent studies combined the inflation testing of human and animal eye globes with the inverse finite element method (IFEM) (Coudrillier et al. 2013, 2012; Girard et al. 2009a; Grytz et al. 2013, 2014), which is a well-accepted method to extract tissue stiffness by minimizing the difference between the model-predicted displacements and the experimentally measured displacements iteratively. However, the accuracy of the ex vivo experiments is inevitably compromised by unphysiological test conditions (Lewis et al. 2014) and IFEM also suffers from a large computational cost due to iterative use of nonlinear FE models (Acton 2012). Alternatively, in vivo extraction of the mechanical properties of the ONH region may offer a more accurate representation. Recent advances in optical coherence tomography (OCT) imaging now enable high-resolution imaging of deep ONH structures (Sigal et al. 2014b). Statistical models based on measured OCT parameters have been used to predict ONH stiffness, stress and deformation (Sigal et al. 2014a). Three-dimensional tracking algorithms have also been applied to OCT data at different IOP levels to quantify full-field ONH displacement in vivo (Girard et al. 2013, 2016). However, none of these studies were able to provide a complete description of the mechanical properties of the ONH tissues, especially the complex anisotropic nonlinear response of collagenous tissues within the ONH.

To extract the mechanical properties of human ONH tissues in vivo, we propose a novel technique that combines ONH displacement tracking results from OCT data with an inverse numerical method called virtual fields method (VFM). VFM extracts constitutive parameters from full-field displacement measurements (Pierron et al. 2006) with superior computation speed, and it has been used to identify the stiffness of human aortic tissues in vitro (Avril et al. 2010; Kim et al. 2012). Our long-term goal is to develop a computational tool to quantify ONH biomechanics in vivo, which can potentially be used clinically for glaucoma diagnosis and patient-specific treatment planning.

2 Methodology

The aim of this paper is to introduce and verify the accuracy of a methodology for extracting the stiffness of ONH tissues from measured displacement fields. This is a typical inverse engineering problem, wherein the constitutive parameters need to be determined based on a known geometry and measured deformation of the material under external loads. In a clinical setting, advanced imaging and computational techniques can be used to obtain the geometry of the ONH and its displacement fields at different IOP levels. Considering that normal eye blinking would increase IOP by more than 10 mmHg (Miller 1967), that a forced squint raised an IOP of about 15–80 mmHg, and that eye rubbing can raise IOP as high as 120–150 mmHg (Coleman and Trokel 1969), we believe that IOP increases in the range of 40–45 mmHg are safe to the patients for the short duration of OCT imaging ($\sim$1 min). Based on this, constitutive parameters in the chosen constitutive models that describe the mechanical response of the ONH tissues can be used to determine the ONH tissue stiffness.

In the real-life scenario, as shown by red arrows in Fig. 1, the 3D geometry and the displacement fields are provided by OCT imaging and three-dimensional tracking algorithms (Girard et al. 2013, 2016), and the IOP is measured using ocular tonometry (Tonnu et al. 2005). However, to verify the accuracy of the proposed VFM technique, simulated displacement and IOP data were used in this paper. As shown by blue arrows in Fig. 1, the verification was done using the following steps:

(1) An anatomically representative finite element (FE) model of the eye (corneo-scleral shell + ONH) was created to simulate the effect of IOP increase on the ONH tissues. This model included predetermined constitutive parameters for each ONH tissue.
(2) The 'artificial' ONH geometry and displacement fields from the simulation in (1) were used as inputs to extract the constitutive parameters with our proposed VFM-based technique.
(3) The extracted constitutive parameters from VFM were compared against the predetermined parameters in the

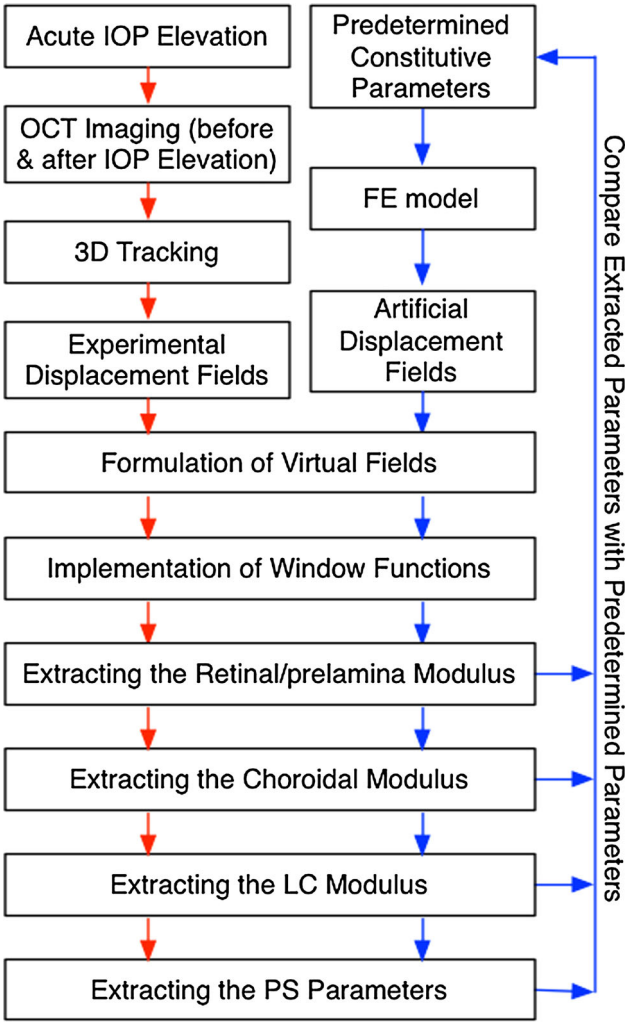

Fig. 1 Flowchart for the implementation of the VFM to extract the mechanical properties of human ONH tissues: (1) *Red arrows* show the clinical scenario and (2) *blue arrows* show the numerical verification scenario

FE model in order to verify the numerical accuracy of VFM.

(4) The robustness of VFM was also tested with added rigid body motions and white noise to the displacement field obtained in (1) and by repeating the steps (2) and (3). The speed of VFM was compared with that of IFEM (Girard et al. 2009a; Grytz et al. 2013).

2.1 Finite element model of the eye

2.1.1 Eye geometry

The posterior half of the eye was modeled as a three-layer axisymmetric half-spherical shell with the center being the origin of the Cartesian coordinate system, and greater details were added to the ONH region (Fig. 2). The three layers—retina, choroid and sclera—were assigned thickness values of 240, 200 and 780 μm, respectively (Manjunath et al. 2010; Norman et al. 2010; Shahidi et al. 1990). The inner radius of the scleral shell was 12 mm. The geometry of the ONH was adapted from the literature (Sigal et al. 2004) and comprised of the LC, prelamina, choroid and peripapillary sclera (PS, the tapered portion of the sclera, 0–1500 μm from the scleral canal). The thickness of the LC and that of the prelamina at the axis of symmetry were 290 and 300 μm, respectively. The radius of curvature of the LC anterior surface was 960 μm. The scleral shell, tapered at the ONH, had a thickness of 430 μm at the canal. In total, 84,640 eight-node hexahedral elements were used to mesh the whole model, with 42,400 elements located at the region of interest—the ONH.

2.1.2 Constitutive models for ocular tissues

Two constitutive models were chosen to describe the mechanical properties of the ocular tissues. For the sclera, which is highly anisotropic and nonlinear (Grytz et al. 2013; Woo et al. 1972), a fiber-reinforced composite model with a constrained von Mises fiber distribution was chosen (Girard et al. 2009b; Gouget et al. 2012). The Cauchy stress tensor for this model is expressed as follows:

$$\sigma = p\mathbf{I} + \frac{2}{J}c_1\left(\widetilde{\mathbf{B}} - \frac{1}{3}\widetilde{I}_1\mathbf{I}\right) + \frac{2}{J}\int_{\theta_p-\pi/2}^{\theta_p+\pi/2} P(\theta,k)\,\widetilde{W}_4(\theta)\widetilde{I}_4(\theta)\left(\mathbf{a}(\theta)\otimes\mathbf{a}(\theta) - \frac{1}{3}\mathbf{I}\right)\mathrm{d}\theta \quad (1)$$

The first right-hand term is the Lagrange multiplier that ensures quasi-incompressibility of the tissue. The second describes the isotropic neo-Hookean response of the ground substance matrix where c_1 is half of the shear modulus. The third term represents the nonlinear and anisotropic behavior of collagen fibers. The collagen fibers have been observed to be tangential to the scleral surface and follow a unimodal distribution within the plane parallel to the scleral surface (Gouget et al. 2012). The constrained von Mises distribution of collagen fibers was used here, and it is expressed as

$$P(\theta,k) = \frac{(1-\beta)}{\pi} + \frac{\beta}{\pi I_0(k)}\exp\left(k\cos\left(2(\theta-\theta_p)\right)\right) \quad (2)$$

where θ_p is the preferred fiber orientation in the local coordinate system. k is the fiber concentration factor which describes the spread of the fiber distribution (illustrated in Fig. 3). β is the proportion of the isotropic subpopulation of collagen fibers that only depends on k. The distribution of collagen fibers is thus determined by θ_p and k only. The strain energy of collagen fibers is

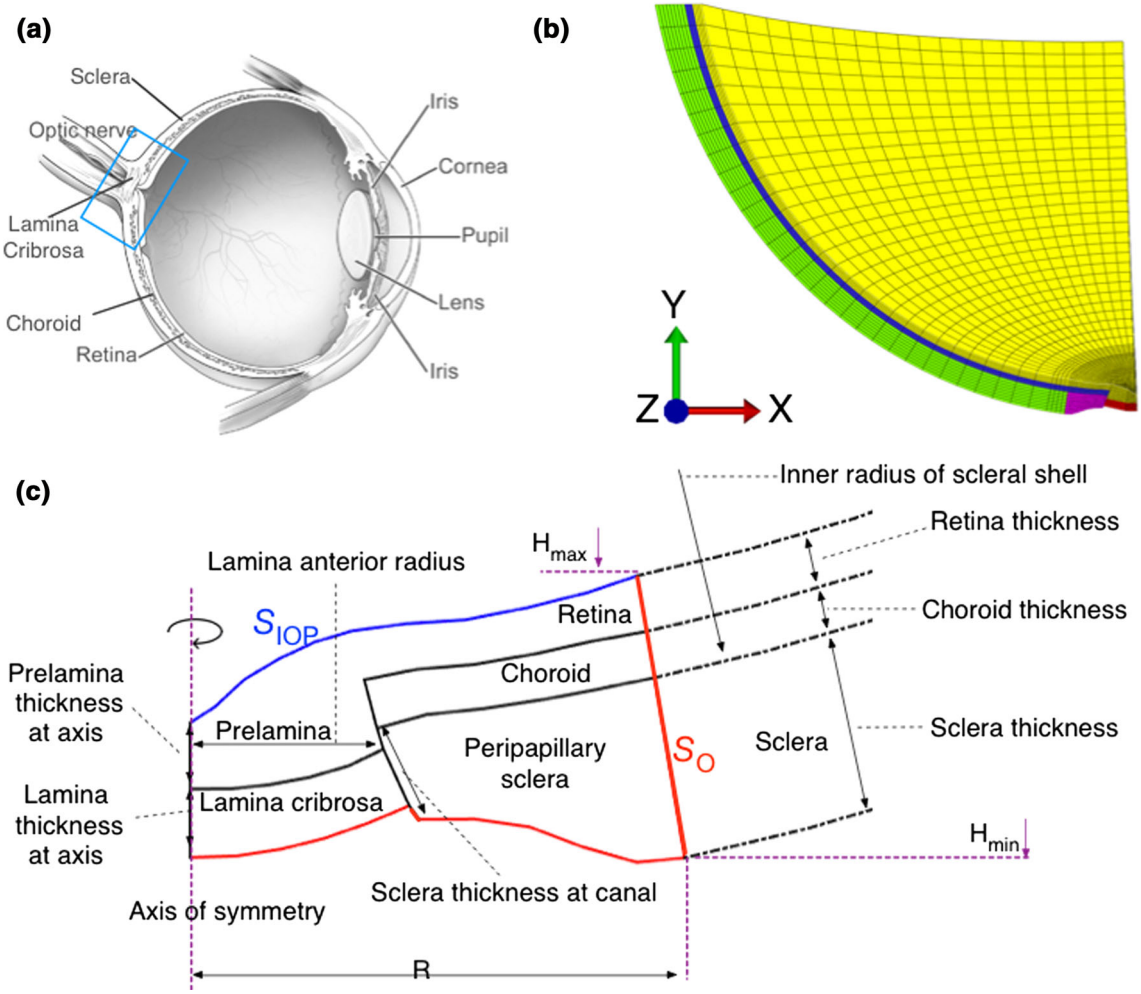

Fig. 2 **a** Schematic of a human eye (adapted from the national eye institute:https://nei.nih.gov/photo/anatomy-of-eye). The ONH region is shown in the *blue rectangle*. **b** Quadrant view of the geometry of the FE model with five different tissues (the retina and the prelamina are shown in *yellow*, the choroid in *blue*, the LC in *red*, the peripapillary sclera in *purple*, and the rest of sclera in *green*). The model is axisymmetric to the *y*-axis and was meshed with eight-noded hexahedral elements. **c** Definitions of geometric features in the FE model. The surface S_{IOP} is shown in *blue*, and the surface S_O in *red*

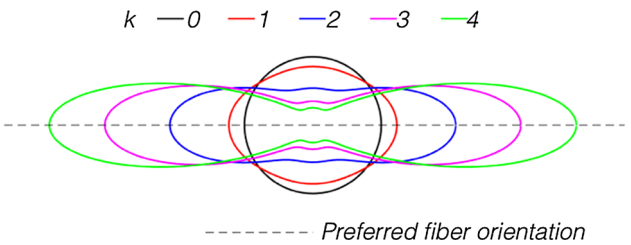

Fig. 3 Polar representation of the constrained von Mises distribution (Gouget et al. 2012) for in-plane scleral collagen fibers with $n = 2$. When the fiber concentration factor k is 0, collagen fibers distribute randomly in the plane parallel to the scleral shell. As k increases, the collagen fibers become aligned along the preferred fiber orientation (here, the *horizontal* direction). When k approaches infinity, this model is equivalent to a transverse isotropic material

$$\widetilde{W}_4(\theta) = \frac{c_3}{2\widetilde{\lambda}(\theta)^2}\left\{\exp\left(c_4\left[\widetilde{\lambda}(\theta) - 1\right]\right) - 1\right\} \tag{3}$$

where c_3 is the exponential fiber stress coefficient, c_4 is the rate of uncrimping collagen fibers, and $\widetilde{\lambda}$ is the fiber stretch. The stiffening of collagen fibers is thus determined by c_3 and c_4. A complete description of this model involves five constitutive parameters: c_1, c_3, c_4, θ_{p} and k.

Other ocular tissues (retina, prelamina, choroid and the LC) were assumed to be neo-Hookean hyperelastic materials. The Cauchy stress tensor is defined as

$$\sigma = \frac{\mu}{J}(\mathbf{B} - \mathbf{I}) + p\mathbf{I} \tag{4}$$

where μ is the shear modulus. p is the hydrostatic pressure to ensure quasi-incompressibility, and it is implemented as $K \cdot \ln(J)/J$.

The values of the constitutive parameters used in the FE model are shown in Table 1. μ_{r}, μ_{c} and μ_{lc} denote the shear modulus for the retina and prelamina, the choroid and the

Table 1 Constitutive parameters input in the FE model to generate simulated displacement fields

Abbreviation	Description	Value
Neo-Hookean hyperelastic material model		
μ_r	Shear modulus for the retina and prelamina	10.07 kPa
μ_c	Shear modulus for the choroid	100.7 kPa
μ_{lc}	Shear modulus for the LC	100.7 kPa
Fiber-reinforced composite material model		
c_1	First Mooney–Rivlin coefficient	100 kPa
c_3	Exponential fiber stress coefficient	5 kPa
c_4	Rate of uncrimping collagen fibers	400
θ_p	Preferred fiber orientation	$\frac{\pi}{2}$ [a]
k_{ps}	Fiber concentration factor for the PS	3
k_s	Fiber concentration factor for scleral shell	0

[a] $\frac{\pi}{2}$ is the circumferential direction

LC, respectively (Chen et al. 2014; Friberg and Lace 1988; Graebel and Van Alphen 1977). The scleral shell and the PS shared the same constitutive properties except for the fiber concentration factors. The PS was considered anisotropic, with $k = 3$ and a circumferential organization, while the rest of the sclera was considered isotropic with $k = 0$ (Eilaghi et al. 2010; Zhang et al. 2015). Note that when k equals 0, θ_p has no influence on the model anymore, based on Eq. 2.

2.1.3 Loading and boundary conditions

The nodes at the equator of the eye model were fixed along the axial direction (Fig. 2, y direction), allowing for free expansion of the equator in the transverse direction (Fig. 2, x and z directions). A linearly increasing pressure load was applied uniformly to the inner surface of the retinal/prelaminar tissues. The maximum pressure was 6 kPa, which is equivalent to an IOP of 45 mmHg.

2.1.4 FE simulation results

The FE solver package FEBio (Musculoskeletal Research Laboratories, University of Utah, Salt Lake City, UT, USA) was used to calculate the IOP-induced displacements of the FE model described above (Maas et al. 2009). The FE model provided simulated displacement fields for the ONH at various IOP levels. Simulation results corresponding to selected IOP levels (using 22.5 mmHg as the first IOP increase and 45 mmHg as the second IOP increase) are shown in Fig. 4.

2.2 Extracting constitutive parameters using the virtual fields method

2.2.1 Governing equation of VFM

VFM is based on the principle of virtual work, which states that when equilibrated forces and stresses in a deformable body undergo any kinematically admissible virtual deformation, the internal virtual work equals the external virtual work. If the body forces are neglected, as assumed for the eye, this principle can be written as:

$$\int_V \sigma\,(\mathbf{p}, \mathbf{u}) : \varepsilon^* \mathrm{d}V = \int_S \mathbf{T} \cdot \mathbf{u}^* \mathrm{d}S \tag{5}$$

where the Cauchy stress σ is a function of unknown constitutive parameters $\mathbf{p}(\mathbf{p} = \left[\mu_r, \mu_c, \mu_{lc}, c_1, c_3, c_4, \theta_p, k\right])$ and the experimentally measured displacement field $\mathbf{u}$; V is the tissue volume, $\mathbf{T}$ is the external force, S is the tissue boundary surface, $\mathbf{u}^*$ is the virtual displacement, and ε^* is the corresponding virtual strain. The latter can be expressed as:

$$\varepsilon^* = \frac{1}{2}\left(\nabla \mathbf{u}^* + \nabla^T \mathbf{u}^*\right) \tag{6}$$

The virtual displacement and strain fields are just mathematical test functions, subject to the geometrical boundary conditions. They have no relation to the actual deformations measured in vivo (Pierron and Grédiac 2012).

Based on Eq. 5, in order to apply VFM to extract the ONH constitutive parameters $\mathbf{p}$, the following must be known: (1) the geometry and the measured displacement field $\mathbf{u}$; (2) the distribution of external forces $\mathbf{T}$; and (3) the virtual displacement field $\mathbf{u}^*$. In this study, the geometry and the measured displacement field were obtained from the FE model (Sect. 2.1).

2.2.2 External forces

The distribution of $\mathbf{T}$ may not be known at every part of the ONH. For instance, for the eye, the only measurable force is IOP; the forces exerted on the posterior surfaces of the peripapillary sclera and LC (e.g., from the cerebrospinal fluid pressure or orbital fat) and the hoop stresses acting on the ONH boundaries are typically unknown (Fig. 2a). Fortu-

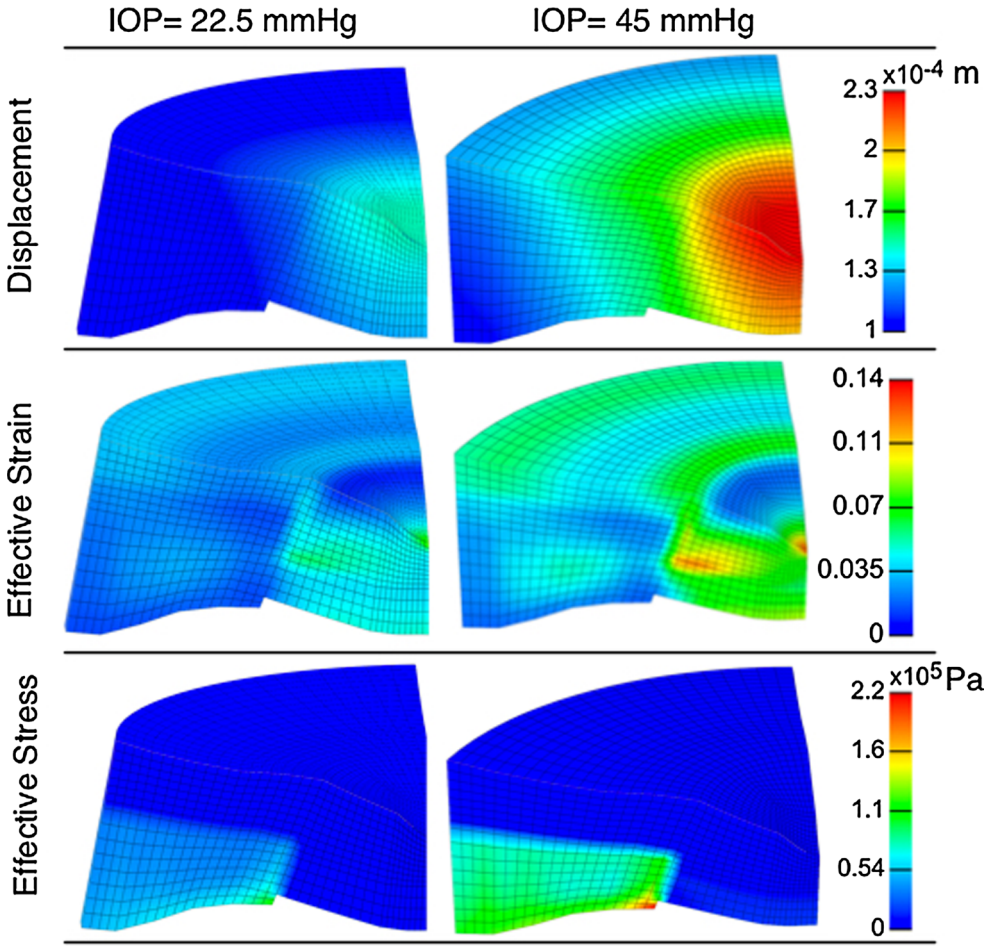

Fig. 4 Simulation results of the FE model for two IOP increases. The displacement, effective strain and effective stress fields of the ONH are displayed as *color* maps for a cropped quadrant only

nately, these unknown boundary forces can be excluded from the calculation of the external virtual work by applying zero virtual surface displacement at the corresponding locations (Toussaint et al. 2006). This is explained using the following equation:

$$\int_V \sigma : \varepsilon^* \mathrm{d}V = \int_S \mathbf{T} \cdot \mathbf{u}^* \mathrm{d}S = \mathrm{IOP} \int_{S_{\mathrm{IOP}}} \mathbf{n} \cdot \mathbf{u}^*_{\mathrm{IOP}} \mathrm{d}S + \int_{S_{\mathrm{O}}} \mathbf{T}_{\mathrm{O}} \cdot \mathbf{u}^*_{\mathrm{O}} \mathrm{d}S \quad (7)$$

where S_{IOP} is the inner surface of the retina and prelamina to which IOP is applied (Fig. 2c), S_{O} represents the surface of the ONH other than S_{IOP} (including the posterior surface of the LC and PS, and the boundary between the ONH and the cornea-scleral shell), $S = S_{\mathrm{IOP}} \cup S_{\mathrm{O}}$, $\mathbf{n}$ is the unit surface normal vector, $\mathbf{T}_{\mathrm{O}}$ represents the unknown boundary forces on S_{O}, $\mathbf{u}^*_{\mathrm{IOP}}$ is the virtual displacement at S_{IOP}, and u^*_{O} is the virtual displacement at S_{O}. If we define $\mathbf{u}^*_{\mathrm{O}} = 0$ over S_{O}, the second right-hand term of Eq. 7 vanishes and $\mathbf{T}_{\mathrm{O}}$ does not contribute to the calculation of the virtual work, as shown here:

$$\int_V \sigma : \varepsilon^* \mathrm{d}V = \mathrm{IOP} \int_{S_{\mathrm{IOP}}} \mathbf{n} \cdot \mathbf{u}^*_{\mathrm{IOP}} \mathrm{d}S \quad (8)$$

As a result, IOP is the only external force that needs to be known to extract the constitutive parameters $\mathbf{p}$. Note that $\mathbf{u}^*_{\mathrm{IOP}}$ should not be zero; otherwise, the external virtual work would be zero, in which case only the relative relationship between the constitutive parameters of different tissues can be derived.

2.2.3 Choosing appropriate virtual fields

The choice of virtual fields is important for accurate extraction of the constitutive parameters especially with noisy data (Avril et al. 2004; Pierron et al. 2006). The virtual displacements must be continuous across the whole ONH volume and meet the prescribed boundary conditions. Methods to create 'optimal virtual fields' that minimize the effect of noisy data have been proposed in the literature for non-iterative VFM and linear constitutive models (Avril and Pierron 2007), but not for nonlinear iterative VFM and hyperelastic materials. The empirical guideline we adopted here is that if the

virtual fields are smooth, the error due to random noise in the displacement measurement can be averaged out. This methodology has been applied in various studies (Avril et al. 2010; Promma et al. 2009; Yoon et al. 2015). Thus, simple functions were used to construct the virtual displacement fields.

Before constructing the virtual displacement fields, a cylindrical coordinate system (r, ω, h) was defined at the ONH for the convenience of calculation:

$$\begin{cases} r = \sqrt{x^2 + z^2} & r \in [0, R] \\ \omega = \text{atan2}\,(z, x) & \omega \in [0, 2\pi) \\ h = y & h \in [H_{\min}, H_{\max}] \end{cases}. \tag{9}$$

where R, $H_{\min}$ and $H_{\max}$ are the boundary coordinate values for nodes located in the ONH (Fig. 2c). atan2 is the arctangent function with two arguments:

$$\text{atan2}(y, x) = \begin{cases} \arctan\left(\frac{y}{x}\right) + \pi & \text{if } x > 0, \\ \arctan\left(\frac{y}{x}\right) + 2\pi & \text{if } x < 0 \text{ and } y \geq 0, \\ \arctan\left(\frac{y}{x}\right) & \text{if } x < 0 \text{ and } y < 0, \\ \frac{3\pi}{2} & \text{if } x = 0 \text{ and } y > 0, \\ \frac{\pi}{2} & \text{if } x = 0 \text{ and } y < 0, \\ \text{undefined} & \text{if } x = 0 \text{ and } y = 0. \end{cases} \tag{10}$$

The virtual displacements were expressed as:

$$\mathbf{u}^* = \left(u_{\mathrm{r}}^* \mathbf{e_r} + r u_{\mathrm{w}}^* \mathbf{e_w} + u_{\mathrm{h}}^* \mathbf{e_h}\right) \boldsymbol{\mathcal{L}} \tag{11}$$

where $\boldsymbol{\mathcal{L}}$ is a scalar window function to enforce the required boundary conditions for the virtual fields. The use of $\boldsymbol{\mathcal{L}}$ is important, especially when analyzing clinical data with complex ONH geometries.

Five virtual displacement fields were used here, as the largest number of unknown constitutive parameters for a single tissue was five. The virtual displacement fields were defined as:

$$\mathbf{u}_1^*: \begin{cases} u_{\mathrm{r}}^* = \frac{\sin(2\pi r/R)(h - H_{\min})}{H_{\max} - H_{\min}} \\ u_{\mathrm{w}}^* = 0 \\ u_{\mathrm{h}}^* = 0 \end{cases}$$

$$\mathbf{u}_2^*: \begin{cases} u_{\mathrm{r}}^* = \frac{r(R-r)\left(\frac{R}{2} - r\right)(h - H_{\min})}{H_{\max} - H_{\min}} \\ u_{\mathrm{w}}^* = 0 \\ u_{\mathrm{h}}^* = 0 \end{cases}$$

$$\mathbf{u}_3^*: \begin{cases} u_{\mathrm{r}}^* = 0 \\ u_{\mathrm{w}}^* = \frac{\sin(2\pi r/R)(h - H_{\min})}{r(H_{\max} - H_{\min})} \\ u_{\mathrm{h}}^* = 0 \end{cases} \tag{12}$$

$$\mathbf{u}_4^*: \begin{cases} u_{\mathrm{r}}^* = 0 \\ u_{\mathrm{w}}^* = \frac{(R-r)\left(\frac{R}{2} - r\right)(h - H_{\min})}{H_{\max} - H_{\min}} \\ u_{\mathrm{h}}^* = 0 \end{cases}$$

$$\mathbf{u}_5^*: \begin{cases} u_{\mathrm{r}}^* = 0 \\ u_{\mathrm{w}}^* = 0 \\ u_{\mathrm{h}}^* = -\frac{\sin\left(\frac{\pi(R-r)}{2R}\right)(h - H_{\min})}{H_{\max} - H_{\min}} \end{cases}$$

Besides being simple and smooth, the proposed virtual fields also accounted for deformations in all directions, thereby allowing for material properties in those directions to be extracted: $\mathbf{u}_1^*$ and $\mathbf{u}_2^*$ are radial (r direction) virtual displacement fields; $\mathbf{u}_3^*$ and $\mathbf{u}_4^*$ are circumferential (ω direction) virtual displacement fields; $\mathbf{u}_5^*$ is an out-of-plane (h direction) virtual displacement field. The proposed virtual displacements were then transformed back to Cartesian coordinates (see Fig. 5 for graphic representations of the virtual displacement fields) and multiplied by the window function $\mathcal{L}$ (defined in Sect. 2.2.4) as in Eq. 11.

2.2.4 Extracting constitutive parameters using VFM

Once we defined the geometry, the displacement, the external forces and the virtual fields, all constitutive parameters $\mathbf{p}$ can be extracted. These parameters were extracted by minimizing the difference between the internal virtual work and the external virtual work using differential evolution—a genetic global optimization algorithm (Price et al. 2006). Differential evolution involves defining a cost function and minimizing it over iterations. Based on Eq. 8, our cost function (internal minus external virtual work) was defined as:

$$\phi\left(\text{IOP}, \mathbf{u}^*, \mathbf{u}\right) = \left| \sum_{i=1}^{N_{\mathrm{e}}} \sigma_i\left(\mathbf{u}\right) : \varepsilon_i^*\left(\mathbf{u}^*\right) V_i - \text{IOP} \sum_{j=1}^{N_{\mathrm{s}}} \mathbf{n}_j \cdot \mathbf{u}_j^* S_j \right| \tag{13}$$

where N_{e} is the number of elements in the ONH, N_{s} is the number of surface elements on S_{IOP}, $\mathbf{n}_j$ is the unit normal surface vector of surface element j. For the numerical implementation, a 2D Gaussian quadrature rule (four points) was used for the surface integral of external virtual work and a 3D Gaussian quadrature rule (eight points) was used for the volume integral of internal virtual work (not shown in Eq. 13 for simplification). When several unknown parameters are to be extracted, multiple virtual fields (typically one virtual field per unknown parameter) are used to ensure the uniqueness of solutions. Multiple displacement fields at different IOP levels can also be incorporated into the cost functions when needed. Thus, a general form of the cost function involving N_{v} virtual fields and N_{IOP} IOP increases was written as:

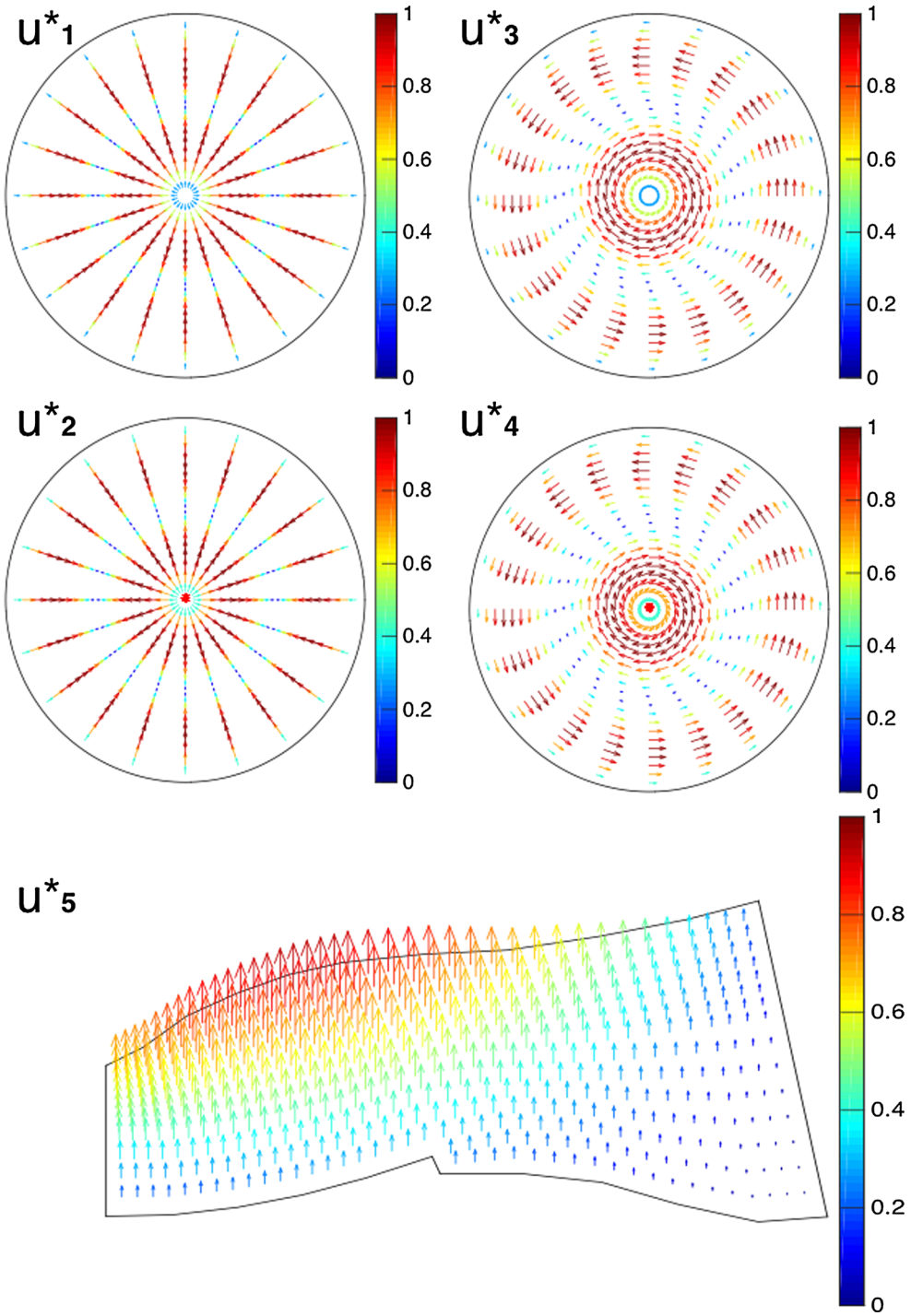

Fig. 5 Graphic representations of the virtual displacement fields. The magnitudes of the virtual displacements were scaled against the maximum value of each virtual displacement field before plotting. The *arrows* represent the virtual displacement vectors, while the lengths and the *colors* of the *arrows* represent the scaled magnitudes. $\mathbf{u}_1^* - \mathbf{u}_4^*$ are plotted in the $x - z$ plane, and $\mathbf{u}_5^*$ is plotted in the $x - y$ plane (as defined in Fig. 2)

$$\Phi = \sum_{m=1}^{N_v} \sum_{n=1}^{N_{IOP}} \phi \left(\mathrm{IOP}_n, \mathbf{u}_m^*, \mathbf{u}_n \right) \tag{14}$$

A minimum of two IOP increases were required to determine the nonlinear stiffening of scleral fibers, and five virtual fields were used to account for five unknowns in the scleral

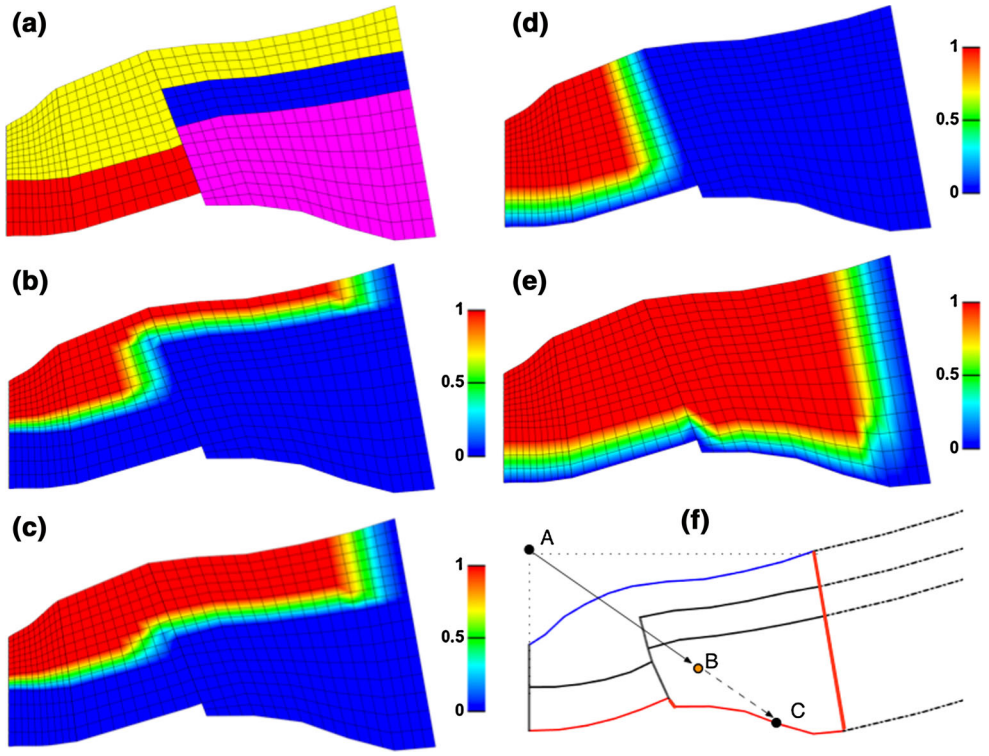

Fig. 6 Window functions (bounded on [0,1]) applied to the proposed virtual fields. **a** Boundaries and regions of different tissues in the ONH. **b** Window function to extract the stiffness of the retina and prelamina. **c** Window function to extract the stiffness of the choroid. **d** Window function to extract the stiffness of the LC. **e** Window function to extract the stiffness of the PS. The window functions were constructed numerically, and the color maps indicate the nodal values of the window functions. **f** Illustration of calculations of window function values in step 4. *Point A* is a fixed starting point aligned with the symmetric axis and H_{max} (defined in Fig 2c). *Point B* is any node in the ONH. *Point C* is the cross-point of *line AB* with the boundary where zero virtual displacement is required (as shown in *red*). To calculate the window function value at *node B*, the ratio of the norm ||CB|| and ||CA|| (defined as ρ, $\rho \in [0, 1]$) is compared with a predefined threshold value η. If $\rho \geq \eta$, the window function value at node B is 1; if $\rho < \eta$, the window function value at *node B* is ρ/η. In this study, η was set to 0.2

constitutive model. This setting ($N_v = 5$, $N_{IOP} = 2$) is consistent throughout this study. The constructed cost function Φ was minimized with respect to the unknown constitutive parameters **p**. However, to reduce the computational cost, we transformed the extraction task to four small problems with fewer unknowns in each step:

1. *Extracting the retinal/prelamina modulus* μ_r We prescribed zero virtual displacements for all nodes outside the retina and prelamina (Fig. 6b). As a result, the internal elastic energy only involved stress in the retina and prelamina (Eq. 5). This reduced the number of unknowns in the cost function (Eq. 14) to one, namely the retinal/prelamina shear modulus μ_r, which was then determined.
2. *Extracting the choroidal modulus* μ_c We prescribed zero virtual displacements for nodes in the PS and LC. The internal elastic energy then involved the stress in the retina, prelamina and choroid. Since the retinal/prelamina modulus had been calculated in the first step, only the choroidal modulus μ_c was unknown in Eq. 14 and could be determined by minimization.
3. *Extracting the LC modulus* μ_{lc} We prescribed nonzero virtual displacements only for nodes inside the prelamina and the LC to calculate the modulus of the LC μ_{lc}.
4. *Extracting the PS parameters* c_1, c_3, c_4, θ_p *and* k We prescribed nonzero virtual displacements for all the nodes inside the ONH and zero virtual displacement at S_O. Then the cost function was minimized to get the constitutive parameters of the PS.

To apply the proposed virtual fields in Eq. 12 in the four-step procedure, a set of four window functions were generated numerically (Fig. 6). Each window function was used in one of the four steps, enforcing the required boundary conditions for the virtual fields. The window functions were defined as unity for a majority of the targeted tissues in each step and gradually decreased to zero at required regions and surfaces. For example, for step one, $\mathcal{L}$ is zero over S_O and zero in the choroid, LC and PS. The proposed functions in Eq. 12 at each node were multiplied by the window function values accordingly, before they were used to calculate the virtual strains. In theory, the virtual displacement was required to be C^0 continuous. It was observed that if the window functions

were not applied, the virtual displacement fields would not be continuous near S_O or tissues where zero virtual displacement had to be enforced, creating high local virtual strains. This led to premature convergence in the DE optimization (data not shown).

2.3 Testing the robustness of VFM

First, the proposed technique was tested against rigid body motions added to the simulated displacement data from the FE model. The displacement field at IOP = 22.5 mmHg underwent a translation of (40, 60, 10) μm and a rotation of $\pi/4$ radians around the y-axis. The displacement field at IOP = 45 mmHg underwent a translation of (10, 30, 50) μm and a rotation of -1.29 radians around the axis $(-1/3, 2/3, 2/3)$.

Second, uniform random noise was added to the simulated displacement data to test the sensitivity of VFM to noise. The magnitude of noise was assessed using the mean of the percentage error in all the strain components in each element at IOP = 45 mmHg. 1% strain noise (equivalent to a 0.04 μm error in displacement) and 4% strain noise (equivalent to a 0.16 μm error in displacement) were used in the test. Five different calculations were performed for each noise level, with each calculation corresponding to one new set of randomly generated noise added to the simulated displacement fields. The average values, the percentage errors of the average values and the coefficients of variation (COVs, ratio of standard deviation to the mean) were reported for the identified constitutive parameters.

2.4 Computational speed comparison between VFM and IFEM

A MATLAB algorithm was written to perform IFEM. For simplicity, we compared the computational speed of step 4 IFEM with that of VFM in extracting a single scleral parameter, c_4. All other constitutive parameters in $\mathbf{p}$ were considered as known. For the IFEM, IOP was applied to S_{IOP} as stress boundary condition; nodal displacements at S_O at IOP = 22.5 mmHg and IOP = 45 mmHg were prescribed as displacement boundary condition; the IFEM cost function was the sum of root mean square of displacement difference of all the nodes in the ONH at the two IOP levels. For fairness of comparison, the same differential evolution algorithm was used to minimize the cost functions for both IFEM and VFM.

2.5 Proof of principle using in vivo clinical data

VFM was implemented on in vivo clinical data from the right eye of one healthy human subject (age: 57; gender: female). The eye was first scanned at baseline IOP (measured to be 17 mmHg) using Spectral-domain OCT (Spectralis; Heidelberg Engineering GmbH, Heidelberg, Germany). The IOP was then gently raised by indenting the anterior sclera through the lower eyelid using an ophthalmodynamometer [(applied force: 0.64 N; see validated protocol in Tun et al. (2016)]. While the indenter was maintained in place, IOP was measured to be 39 mmHg with a Tonopen and a second OCT scan was performed. Digital reconstruction of the ONH tissues (Fig. 7a) and three-dimensional tracking algorithms were used to calculate the IOP-induced displacements of the visible portions of the prelamina and LC between the two OCT volumes using established protocols (Girard et al. 2013, 2016). A central region which included most of the visible prelamina and LC was selected as the region of interest (Fig. 7b) to calculate the biomechanical properties of the prelamina and LC using the proposed procedures in Sect. 2.2. To eliminate noise, the displacement field from tracking was smoothed by a seventh-order polynomial fitting in 3D (Midgett et al. 2017; Promma et al. 2009) before being used in the VFM (Fig. 7c). For simplicity, all tissues were assumed to be incompressible. Therefore, the Jacobian J was set to 1 for all elements, thus eliminating the need to include the volumetric stress in the virtual work calculation.

3 Numerical results

The FE displacement fields at IOP = 22.5 mmHg and IOP = 45 mmHg were used as inputs for the VFM technique, and our VFM extraction results are reported in Table 2.

Specifically, the obtained constitutive parameters matched well with the predetermined input parameters (reference, Table 2). The percentage errors were less than 0.01% for the neo-Hookean tissues (retina, prelamina, choroid and LC) and less than 0.05% for the fiber-reinforced PS (without noise, Table 2).

The constitutive parameters obtained from displacement fields with rigid body motions were comparable with those obtained from the original displacement fields. The percentage errors were also less than 0.05% for all parameters (with rigid body motion, Table 2).

The mean of constitutive parameters obtained from displacement fields with noise fell near the reference values. With 1% strain noise, percentage errors were less than 0.1% for the neo-Hookean tissues and less than 5% for the sclera. With 4% strain noise, percentage errors were less than 0.5% for the neo-Hookean tissues and less than 2% for the sclera. The COVs for each of the identified constitutive parameters increased as the noise level increases (1% strain noise and 4% strain noise, Table 2).

The CPU time for each of the four steps in our proposed VFM technique was 28, 36, 28 and 17,851 s, respectively (iMac, 2.9 GHz quad-core Intel Core i5, parallelized on four CPU cores). The total RAM usage was 239.4 MB.

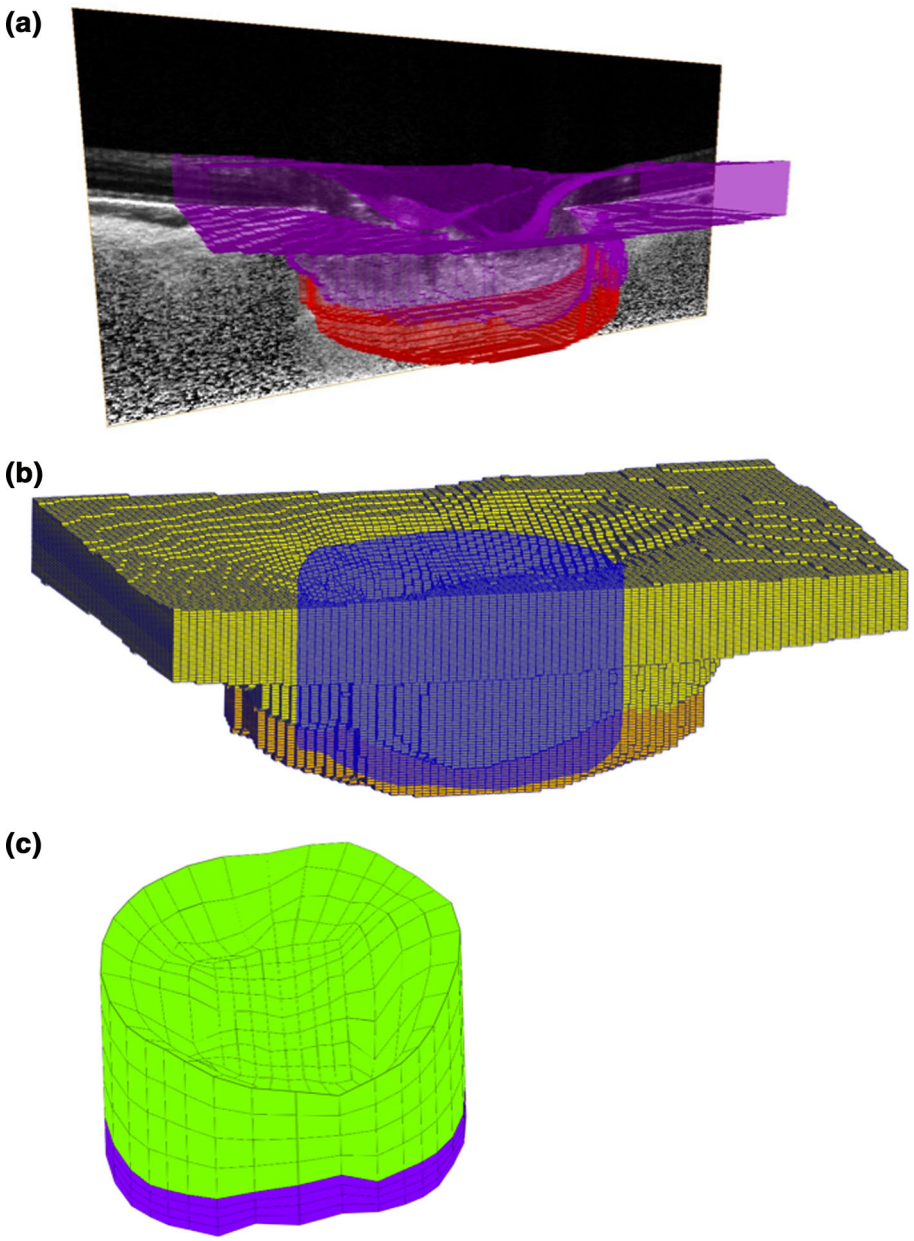

Fig. 7 **a** Digital reconstruction of the prelamina and LC from the OCT volume of one healthy subject's ONH. **b** The relative position between the region of interest used in VFM (shown in *blue*) and the segmented ONH geometry (retina/prelamina shown in *yellow*, LC shown in *orange*). **c** Mesh used in the VFM

Computational speeds for the VFM and IFEM techniques are shown in Table 3. The accuracies of the two methods were equivalently good. However, VFM was found to be 125 times faster than IFEM.

The estimated shear modulus for prelamina and LC of the studied subject's eye were 33.7 and 63.5 kPa, respectively.

4 Discussion

In this study, we proposed a four-step procedure based on VFM to extract the constitutive parameters of human ONH tissues. We created a FE model to provide simulated displacement, geometry and IOP data, and verified the accuracy of the proposed VFM technique in extracting ONH constitutive parameters. We tested the sensitivity of the technique to rigid body motions and noise added to the displacement data. Our principal findings are as follows: First, VFM was capable of identifying hyperelastic constitutive parameters of human ONH tissues despite the complex geometry and loading conditions. Second, knowledge of IOP is sufficient for the extraction of ONH stiffness using VFM. Third, VFM was insensitive to ONH rigid body motions. Fourth, VFM captured the complex mechanical characteristics even in the presence of noise. Fifth, VFM was significantly faster than IFEM. Sixth, the ONH was found to be an excellent candidate

Table 2 Extracted constitutive parameters using VFM

	μ_r (kPa)	μ_c (kPa)	μ_{lc} (kPa)	c_1 (kPa)	c_3 (kPa)	c_4	θ_p	k
Reference	10.07	100.7	100.7	100	5	400	$\pi/2$	3
Without noise	10.07	100.7	100.7	99.97	5.001	400.0	1.571	3.000
Percentage error	0.001%	0.010%	0.004%	0.034%	0.027%	0.006%	0.000%	0.007%
With rigid body motion	10.07	100.7	100.7	99.97	5.001	400.0	1.5708	3.000
Percentage error	0.001%	0.012%	0.008%	0.031%	0.021%	0.004%	0.000%	0.009%
1% Strain noise								
Mean	10.07	100.8	100.7	104.3	4.838	402.7	1.570	2.974
Percentage error	0.000%	0.070%	0.001%	4.26%	3.24%	0.685%	0.001%	0.859%
COV (%)	0.013	0.205	0.172	3.64	2.45	0.479	0.024	0.933
4% Strain noise								
Mean	10.07	100.6	100.2	99.40	4.953	399.4	1.572	3.042
Percentage error	0.006%	0.052%	0.496%	0.604%	0.948%	0.161%	0.134%	1.41%
COV (%)	0.117	0.837	0.774	8.91	6.36	1.44	0.053	2.79

Table 3 Computational speed comparison between VFM and IFEM

	Extracted c_4	Number of iterations in DE[a]	CPU time (s)
VFM	400.00	82	281
IFEM	400.00	31	35,147

[a] A population size of 12 was used for each differential evolution iteration for both methods. Tests were performed on an iMac (2.9 GHz quad-core Intel Core i5)

for VFM. Seventh, the implementation of VFM on in vivo data demonstrates the feasibility of VFM. As a result of these findings, VFM may be of interest for clinical translation.

4.1 VFM can accommodate complex geometry, biomechanical properties and loading conditions

With displacement fields at IOP = 22.5 and 45 mmHg, the extracted constitutive parameters matched well with the reference values. The percentage errors were less than 0.01% for the neo-Hookean tissues and less than 0.05% for the fiber-reinforced PS, showing that the chosen hyperelastic constitutive models were compatible with VFM.

Most of the VFM studies in the literature dealt with engineering structures prepared in designed shapes and tested with chosen loading conditions (for example, planar deformation of rubber sheet (Guélon et al. 2009), three-point bending impact test on an aluminum bar (Pierron et al. 2011), Arcan loading tests of PVC foam (Wang et al. 2013)). On the contrary, for the ONH, we have no control over its geometry, and to date, the only loading condition affecting the ONH tissues that can be easily manipulated and measured clinically is the IOP. The ONH has a complex geometry, comprising of several structurally and biomechanically distinct tissues. As a result, the magnitude of strain and stress distributions also varied from tissue to tissue in the FE model (Fig. 4). In spite of this, our VFM-based technique was able to identify the stiffness of these tissues one by one with good accuracy. In the clinical scenario, the deeper portions of the sclera/LC might not be visible in the OCT volume. Accordingly, the window function could be easily adjusted to apply zero virtual displacements at the boundary between the visible portion and invisible portion. Doing so will cancel out the influence of invisible structures. The extracted parameters will then represent the material properties of the visible ONH tissues only.

4.2 Knowledge of IOP is sufficient for the extraction of ONH stiffness using VFM

Throughout the day and night, the ONH is exposed to fluctuations in three major mechanical loads: the intraocular pressure, pushing the ONH away from the center of the eye; the cerebrospinal fluid pressure, pushing the ONH toward the center of the eye (Morgan et al. 1995; Ren et al. 2010); and during eye movements, the traction from the optic nerve sheaths that could result in even larger ONH deformations (Wang 2016). These loads may also generate large hoop stresses acting at the boundaries of the ONH tissues. It needs to be emphasized that none of these loads and stresses can be measured in vivo in a clinical setting, except for IOP. However, in our study, we proposed a novel VFM approach that only required knowledge of IOP. Specifically, the unknown forces were excluded from the calculation of external virtual work by applying zero virtual displacement on S_O, which was

enforced by the use of window functions (Fig. 6) applied to the virtual displacement fields. In other words, knowledge of a subject's baseline IOP and its increase (as currently achievable clinically) is sufficient to extract the stiffness of ONH tissues in vivo. This has important implications for translating VFM into clinical practice.

4.3 VFM was insensitive to ONH rigid body motions

When imaging the ONH structures of the eye in a clinical setting, changes in orientation of the eye and patient head movements may result in rigid body motions across different scans. For traditional IFEM, rigid body motions in the displacement fields must be first filtered (Jordan et al. 2009; Moerman et al. 2009). For the ONH, it is standard practice to align Bruch's membrane opening planes across ONH volumes to remove rigid body motions (Johnstone et al. 2014). However, this is under the assumption that ONH tissues other than Bruch's membrane follow the exact same rigid body motion transformation, which is intrinsically inaccurate. In our study, we found that VFM was insensitive to rigid body motions added to the displacement fields. This is because the VFM used relative nodal displacements in each element to calculate the stress in the cost function, while for IFEM, absolute values of displacement obtained from experiments were directly compared with those from simulations. As a result, VFM can be considered more robust than IFEM, as it does not require the removal of rigid body motions.

4.4 VFM captured the complex mechanical characteristics of the ONH even in the presence of noise

When no noise was present in the displacement data, VFM was compatible with complex hyperplastic constitutive models (employed herein) as demonstrated by the small errors in the constitutive parameters (<0.05%). Even in the presence of 4% strain noise, the percentage errors for the mean of the identified constitutive parameters for the retina, prelamina, choroid and LC were still less than 1% (so were the COVs), showing good stability with regard to noise. For the sclera and in the presence of noise, we found that the constitutive parameters were more prone to errors than those for the neo-Hookean tissues (retina, prelamina, choroid and LC). It has been reported in the literature that VFM applied to highly anisotropic materials may result in large errors in the identified constitutive parameters (Pierron et al. 2000; Toussaint et al. 2006). Interestingly, for the sclera, the microstructural parameters related to anisotropy (θ_p and k) were better extracted (smaller percentage errors and COVs) than those describing the stretch-induced stiffening of the collagen fibers (c_3 and c_4). Note that the worst extraction occurred for the identification of c_1 with COV being 9% for 4% strain noise. However, note that c_1—representing the ground substance matrix of the sclera—has the lowest contribution to the overall scleral stiffness; thus, the effect of c_1 on the total response of sclera to IOP elevation is comparably small. Nonetheless, in the presence of 4% strain noise, the mean percentage errors for the identified constitutive parameters were mostly less than 1%, implying the nonlinearity and anisotropy of the sclera were still well captured.

4.5 VFM was significantly faster than IFEM

The major difference between VFM and IFEM is that VFM calculates the difference between the internal and external virtual works (fast calculation), while IFEM needs to run a new FE model for each newly guessed set of constitutive parameters. For the extraction of c_4, the CPU time for VFM was only 281 s, 125 times faster than IFEM, whose CPU time was 35,147 s. This large difference is due to the fact that every FE model in IFEM requires the formulation and inversion of a large tangent stiffness matrix, and in most cases, multiple time steps are required. In some cases, the tangent stiffness matrix needs to be reformed several times before convergence is reached. All these factors contribute to the large computational cost of IFEM. Furthermore, it is well known that the CPU time and the RAM usage of a FE model are proportional to dof^{α}, where dof is the number of total degrees of freedom in the model and α is a constant ranging from 2 to 3, depending on the solvers used in the FE package (Liu and Quek 2013). Since IFEM is a method to run FE models iteratively, the CPU time for IFEM also increases exponentially as the number of elements increases. On the contrary, the CPU time and RAM usage of our proposed VFM technique are linearly proportional to the number of elements used. In other words, the finer the mesh, the faster the VFM will be, in comparison with IFEM.

Due to the parallelized nature of differential evolution, using a computing cluster with more CPU cores can considerably reduce the CPU time. The same VFM extraction procedure for the sclera took only 2184 s on a 28 CPU cores cluster (Intel Xeon E5-2695 v3 2.3 GHz), compared with 17,851 s using a quad-core iMac machine. The proposed VFM technique has also very low requirements for RAM usage in both cases.

In our four-step procedure, most of the computational time was spent on the extraction of scleral constitutive parameters. This is due to two reasons: First, the fiber-reinforced model is much more complex than the neo-Hookean model; thus, more computing operations are needed to calculate the stress values for each element; second, five unknowns were extracted at the same time for the sclera while only one being unknown for any other tissue. It is known that for global optimization problems, the number of evaluations increases exponentially with the number of variables (Das et al. 2005).

4.6 The ONH is an excellent candidate for VFM

In typical VFM problems, the exact distribution of tractions over the external surface of the interested body is unknown, and only the total force is measurable. For instance, in a uniaxial tensile test, the total force exerted on the clamped end of the specimen is measured by the load cell, but the stresses at the clamped end are not necessarily uniform (Grédiac and Pierron 2006). For these problems, to calculate the external virtual work in Eq. 5, the virtual displacements are restricted to be uniform over the surface where the total force is measured (Hao et al. 2016). However, this constraint can be relaxed when it comes to the identification of ONH constitutive parameters. This is because the only external load used in the calculation of the external virtual work is hydrostatic pressure (IOP) and its distribution was assumed uniform over the retina and prelamina inner surfaces. Thus, the virtual displacement fields we used in this study were not required to be uniform on S_{IOP}. This is a considerable advantage when constructing virtual fields.

4.7 Application of VFM to in vivo deformation data

The proposed VFM method estimated the shear modulus of the prelamina and LC of the studied subject's eye to be 33.7 and 63.5 kPa, respectively. This corresponds to an elastic modulus of 100.3 kPa for the prelamina and of 189.1 kPa for the LC. The prelamina elastic modulus fell within the range of literature values [20–125 kPa (Chen et al. 2014; Chen and Weiland 2010, 2012; Jones et al. 1992)]. The LC was also found stiffer than the prelamina, which can be explained by the presence of collagen fibers and microcapillaries in the LC. The LC elastic modulus also fell within the range of literature values [100–400 kPa (Bellezza 2002; Edwards and Good 2001; Spoerl et al. 2005)]. This proof of principle demonstrates that our custom VFM method may be applicable to clinical data in the near future, but further validations are warranted.

4.8 Limitations

In this study, the following limitations need to be discussed. First, the proposed VFM procedure has to be based on geometry digitally reconstructed from in vivo medical images (e.g., OCT), in which case the prestressed configuration (at IOP = 0 mmHg) will not be available. Our current analysis has to treat the ONH geometry when the eye is subjected to normal IOP (~15 mmHg) as the prestressed configuration, and increases the IOP level twice from this point (currently achievable in vivo). Even for in vitro inflation experiments, a minimum IOP of 5 mmHg is sometimes required to keep the normal eye shape (Girard et al. 2009b). As a result, the identified constitutive parameters for the sclera may overestimate its stiffness, but they will still be representative and meaningful for interpreting in vivo ONH biomechanics across pathologies. In the literature, methods using 'deposition stretch' have been proposed to incorporate the prestress in arterial walls (Bellini et al. 2014). Future research is necessary to incorporate the prestressed configuration (at IOP = 0 mmHg) in ocular biomechanics.

Second, in this paper, we assumed a simple collagen fiber ring pattern in the peripapillary sclera, while studies have shown that the microstructure of the sclera is more complex and can vary significantly with location (Coudrillier et al. 2013; Danford et al. 2013; Grytz et al. 2013; Zhang et al. 2015). A recent study characterized the regional variations in the material properties of murine aortas using specially designed virtual fields (Bersi et al. 2016), in which the displacement data were obtained from ex vivo inflation experiments. Currently, our method has the potential to extract the local material properties by using deformation data from smaller volumes within the ONH. However, further investigation is warranted to test the feasibility and accuracy.

Third, two IOP increases are needed for the identification of nonlinear constitutive parameters. Such a scenario has been achieved successfully in vivo in our recent publication using ophthalmodynamometry (Tun et al. 2016). If displacement data are only available for one IOP increase, a neo-Hookean or orthotropic elastic constitutive model could be used for the sclera. The linear moduli that can be obtained from these models may remain representative of scleral stiffness for a given small IOP range.

Fourth, the virtual fields were constructed based on empirical guidelines and may not be the optimal choice. To cancel the distribution of unknown forces in the equilibrium, the virtual displacements were defined as zero (as enforced by the window function $\mathcal{L}$) on S_{O}, which constrained the formulation of the virtual fields. Even though with artificial displacement and implemented noise model, the accuracy of extraction was not affected by this constrain, further investigation with clinical in vivo data may be necessary to identify virtual fields that are less sensitive to noise.

Fifth, the computational speed comparison between VFM and IFEM was based on a simplified test case scenario in which only one scleral constitutive parameter was considered unknown. Further comparison tests with more constitutive parameters may be warranted.

Finally, in this study, we have only demonstrated the feasibility of VFM by extracting the stiffness of the prelamina and of the LC for a single human subject's eye. For simplicity, we assumed that both tissues were incompressible to eliminate the need to include the volumetric stress in the virtual work calculation. Further studies using more in vivo data and to extract the stiffness of all ONH tissues (including the choroid and sclera) are warranted.

5 Conclusions

In this study, we have proposed and verified a novel technique based on VFM aimed to extract the constitutive parameters of human ONH tissues in vivo. VFM was shown to be compatible with the selected hyperelastic constitutive models. Results showed that the technique was able to accurately capture the nonlinearity and anisotropy of ONH tissues using several test case scenarios. The proposed technique was also found faster and more robust than the gold-standard IFEM. A proof of principle of the VFM was demonstrated by extracting the biomechanical properties of the prelamina and LC of a single subject's eye. Our VFM approach requires further validations with ex vivo and in vivo data. It may have potential in identifying patients' in vivo ONH biomechanical properties if combined with in vivo optical coherence tomography (OCT) images.

Acknowledgements This study was supported by the Ministry of Education, Academic Research Funds, Tier 1 (R-397-000-181-112; Girard) and an NUS Young Investigator Award (NUSYIA_FY13_P03, R-397-000-174-133; Girard).

References

Acton QA (2012) Issues in biomedical engineering research and application. Scholarly Editions, Atlanta

Avril S, Badel P, Duprey A (2010) Anisotropic and hyperelastic identification of in vitro human arteries from full-field optical measurements. J Biomech 43:2978–2985. doi:10.1016/j.jbiomech.2010.07.004

Avril S, Grediac M, Pierron F (2004) Sensitivity of the virtual fields method to noisy data. Comput Mech 34:439–452. doi:10.1007/s00466-004-0589-6

Avril S, Pierron F (2007) General framework for the identification of constitutive parameters from full-field measurements in linear elasticity. Int J Solids Struct 44:4978–5002

Balaratnasingam C, Morgan WH, Bass L, Matich G, Cringle SJ, Yu D-Y (2007) Axonal transport and cytoskeletal changes in the laminar regions after elevated intraocular pressure. Investig Ophthalmol Vis Sci 48:3632–3644

Bellezza A (2002) Biomechanical properties of the normal and early glaucomatous optic nerve head: an experimental and computational study using the monkey model. Department of Biomedical Engineering, Tulane University, New Orleans

Bellini C, Ferruzzi J, Roccabianca S, Di Martino E, Humphrey J (2014) A microstructurally motivated model of arterial wall mechanics with mechanobiological implications. Ann Biomed Eng 42:488–502

Bersi MR, Bellini C, Di Achille P, Humphrey JD, Genovese K, Avril S (2016) Novel methodology for characterizing regional variations in the material properties of murine aortas. J Biomech Eng 138:071005

Burgoyne CF, Crawford Downs J, Bellezza AJ, Francis Suh J-K, Hart RT (2005) The optic nerve head as a biomechanical structure: a new paradigm for understanding the role of IOP-related stress and strain in the pathophysiology of glaucomatous optic nerve head damage. Prog Retinal Eye Res 24:39–73

Chen K, Rowley AP, Weiland JD, Humayun MS (2014) Elastic properties of human posterior eye. J Biomed Mater Res Part A 102:2001–2007

Chen K, Weiland JD (2010) Anisotropic and inhomogeneous mechanical characteristics of the retina. J Biomech 43:1417–1421

Chen K, Weiland JD (2012) Mechanical characteristics of the porcine retina in low temperatures. Retina 32:844–847

Coleman DJ, Trokel S (1969) Direct-recorded intraocular pressure variations in a human subject. Arch Ophthalmol 82:637–640

Coudrillier B, Boote C, Ha Quigley, Nguyen TD (2013) Scleral anisotropy and its effects on the mechanical response of the optic nerve head. Biomech Model Mechanobiol 12:941–963. doi:10.1007/s10237-012-0455-y

Coudrillier B, Tian J, Alexander S, Myers KM, Ha Quigley, Nguyen TD (2012) Biomechanics of the human posterior sclera: age- and glaucoma-related changes measured using inflation testing. Investig Ophthalmol Vis Sci 53:1714–1728. doi:10.1167/iovs.11-8009

Danford FL, Yan D, Dreier RA, Cahir TM, Girkin CA, Geest JPV (2013) Differences in the region-and depth-dependent microstructural organization in normal versus glaucomatous human posterior scleraemicrostructural organization of human posterior sclerae. Investig Ophthalmol Vis Sci 54:7922–7932

Das S, Konar A, Chakraborty UK (2005) Two improved differential evolution schemes for faster global search. In: Proceedings of the 7th annual conference on Genetic and evolutionary computation. ACM, pp 991–998

Edwards ME, Good TA (2001) Use of a mathematical model to estimate stress and strain during elevated pressure induced lamina cribrosa deformation. Curr Eye Res 23:215–225

Eilaghi A, Flanagan JG, Tertinegg I, Simmons CA, Brodland GW, Ethier CR (2010) Biaxial mechanical testing of human sclera. J Biomech 43:1696–1701

Friberg TR, Lace JW (1988) A comparison of the elastic properties of human choroid and sclera. Exp Eye Res 47:429–436

Geraghty B, Jones SW, Rama P, Akhtar R, Elsheikh A (2012) Age-related variations in the biomechanical properties of human sclera. J Mechan Behav Biomed Mater 16:181–191

Girard MJ, Strouthidis NG, Desjardins A, Mari JM, Ethier CR (2013) In vivo optic nerve head biomechanics: performance testing of a three-dimensional tracking algorithm. J R Soc Interface 10:20130459

Girard MJ et al (2016) In vivo 3-dimensional strain mapping of the optic nerve head following intraocular pressure lowering by trabeculectomy. Ophthalmology 123:1190–1200

Girard MJa, Downs JC, Bottlang M, Burgoyne CF, Suh J-KF (2009a) Peripapillary and posterior scleral mechanics-part II: experimental and inverse finite element characterization. J Biomech Eng 131:051012. doi:10.1115/1.3113683

Girard MJa, Downs JC, Burgoyne CF, Suh J-KF (2009b) Peripapillary and posterior scleral mechanics-part I: development of an anisotropic hyperelastic constitutive model. J Biomech Eng 131:051011. doi:10.1115/1.3113682

Gouget CLM, Girard MJ, Ethier CR (2012) A constrained von Mises distribution to describe fiber organization in thin soft tissues. Biomech Model Mechanobiol 11:475–482. doi:10.1007/s10237-011-0326-y

Graebel W, Van Alphen G (1977) The elasticity of sclera and choroid of the human eye, and its implications on scleral rigidity and accommodation. J Biomech Eng 99:203–208

Grédiac M, Pierron F (2006) Applying the virtual fields method to the identification of elasto-plastic constitutive parameters. Int J Plast 22:602–627

Grytz R et al (2013) Material properties of the posterior human sclera. J Mech Behav Biomed Mater 29:602–617. doi:10.1016/j.jmbbm.2013.03.027

Grytz R, Fazio MA, Libertiaux V, Bruno L, Gardiner S, Girkin CA, Downs JC (2014) Age-and race-related differences in human scleral material propertiesscleral material property changes with age and race. Investig Ophthalmol Vis Sci 55:8163–8172

Guélon T, Toussaint E, Le Cam J-B, Promma N, Grediac M (2009) A new characterisation method for rubber. Polym Test 28:715–723

Hao W, Zhang Y, Yuan Y (2016) Eigenfunction virtual fields method for thermo-mechanical parameters identification of composite materials. Polym Test 50:224–234

Heijl A, Leske MC, Bengtsson B, Hyman L, Bengtsson B, Hussein M (2002) Reduction of intraocular pressure and glaucoma progression: results from the Early Manifest Glaucoma Trial. Arch Ophthalmol 120:1268–1279

Johnstone J et al (2014) Variation of the axial location of bruch's membrane opening with age, choroidal thickness race effect of age on Bruch's membrane opening position. Investig Ophthalmol Vis Sci 55:2004–2009

Jones I, Warner M, Stevens J (1992) Mathematical modelling of the elastic properties of retina: a determination of Young's modulus. Eye 6:556–559

Jordan P, Socrate S, Zickler T, Howe R (2009) Constitutive modeling of porcine liver in indentation using 3D ultrasound imaging. J Mechan Behav Biomed Mater 2:192–201

Kim J-H, Avril S, Duprey A, Favre J-P (2012) Experimental characterization of rupture in human aortic aneurysms using a full-field measurement technique. Biomech Model Mechanobiol 11:841–853

Leske MC, Wu S-Y, Hennis A, Honkanen R, Nemesure B (2008) Risk factors for incident open-angle glaucoma: the Barbados eye studies. Ophthalmology 115:85–93

Lewis JA, Garcia MB, Rani L, Wildsoet CF (2014) Intact globe inflation testing of changes in scleral mechanics in myopia and recovery. Exp Eye Res 127:42–48

Liu G-R, Quek SS (2013) The finite element method: a practical course. Butterworth-Heinemann, Oxford

Maas SA, Ellis BJ, Rawlins DS, Weiss JA (2009) A comparison of FEBio, ABAQUS, and NIKE3D. Results for a suite of verification problems. PhD dissertation, University of Utah

Manjunath V, Taha M, Fujimoto JG, Duker JS (2010) Choroidal thickness in normal eyes measured using Cirrus HD optical coherence tomography. Am J Ophthalmol 150(325–329):e321

Midgett DE, Pease ME, Quigley HA, Patel M, Franck C, Nguyen TD (2017) Regional variations in the mechanical strains of the human optic nerve head. In: Mechanics of biological systems and materials, vol 6. Springer, pp 119–127

Miller D (1967) Pressure of the lid on the eye. Arch Ophthalmol 78:328–330

Moerman KM, Holt CA, Evans SL, Simms CK (2009) Digital image correlation and finite element modelling as a method to determine mechanical properties of human soft tissue in vivo. J Biomech 42:1150–1153

Morgan WH, Yu D-Y, Cooper RL, Alder VA, Cringle SJ, Constable IJ (1995) The influence of cerebrospinal fluid pressure on the lamina cribrosa tissue pressure gradient. Investig Ophthalmol Vis Sci 36:1163–1172

Norman RE et al (2010) Dimensions of the human sclera: thickness measurement and regional changes with axial length. Exp Eye Res 90:277–284

Pierron F, Avril S, Toussaint E, Gre M (2006) The virtual fields method for extracting constitutive parameters from full-field measurements: a review. Strain 42:233–253

Pierron F, Grédiac M (2012) The virtual fields method: extracting constitutive mechanical parameters from full-field deformation measurements. Springer, Berlin

Pierron F, Sutton M, Tiwari V (2011) Ultra high speed DIC and virtual fields method analysis of a three point bending impact test on an aluminium bar. Exp Mech 51:537–563

Pierron F, Zhavoronok S, Grédiac M (2000) Identification of the through-thickness properties of thick laminated tubes using the virtual fields method. Int J Solids Struct 37:4437–4453

Price K, Storn RM, Lampinen JA (2006) Differential evolution: a practical approach to global optimization. Springer, Berlin

Promma N, Raka B, Grediac M, Toussaint E, Le Cam J-B, Balandraud X, Hild F (2009) Application of the virtual fields method to mechanical characterization of elastomeric materials. Int J Solids Struct 46:698–715

Quigley HA (2005) Glaucoma: macrocosm to microcosm the Friedenwald lecture. Investig Ophthalmol Vis Sci 46:2663–2670

Ren R et al (2010) Cerebrospinal fluid pressure in glaucoma: a prospective study. Ophthalmology 117:259–266

Resnikoff S, Pascolini D, Etya'ale D, Kocur I, Pararajasegaram R, Pokharel GP, Mariotti SP (2004) Global data on visual impairment in the year 2002. Bull World Health Organ 82:844–851

Schultz DS, Lotz JC, Lee SM, Trinidad ML, Stewart JM (2008) Structural factors that mediate scleral stiffness. Invest Ophthalmol Vis Sci 49:4232–4236

Shahidi M, Zeimer RC, Mori M (1990) Topography of the retinal thickness in normal subjects. Ophthalmology 97:1120–1124

Sigal IA, Flanagan JG, Tertinegg I, Ethier CR (2004) Finite element modeling of optic nerve head biomechanics. Investig Ophthalmol Vis Sci 45:4378–4387. doi:10.1167/iovs.04-0133

Sigal IA, Grimm J, Schuman J, Kagemann L, Ishikawa H, Wollstein G (2014a) A method to estimate biomechanics and mechanical properties of optic nerve head tissues from parameters measurable using optical coherence tomography. IEEE Trans Med Imaging. doi:10.1109/TMI.2014.2312133

Sigal IA, Wang B, Strouthidis NG, Akagi T, Girard MJ (2014b) Recent advances in OCT imaging of the lamina cribrosa. Br J Ophthalmol 98:ii34–ii39

Sommer A, Tielsch JM, Katz J, Quigley HA, Gottsch JD, Javitt J, Singh K (1991) Relationship between intraocular pressure and primary open angle glaucoma among white and black Americans: the Baltimore Eye Survey. Arch Ophthalmol 109:1090–1095

Spoerl E, Boehm AG, Pillunat LE (2005) The influence of various substances on the biomechanical behavior of lamina cribrosa and peripapillary sclera. Investig Ophthalmol Vis Sci 46:1286–1290

Tonnu P, Ho T, Sharma K, White E, Bunce C, Garway-Heath D (2005) A comparison of four methods of tonometry: method agreement and interobserver variability. Br J Ophthalmol 89:847–850

Toussaint E, Grédiac M, Pierron F (2006) The virtual fields method with piecewise virtual fields. Int J Mech Sci 48:256–264. doi:10.1016/j.ijmecsci.2005.10.002

Tun TA, Thakku SG, Png O, Baskaran M, Htoon HM, Sharma S, Nongpiur M, Cheng CY, Aung T, Strouthidis N, Girard MJA (2016) Shape changes of the anterior lamina cribrosa in normal, ocular hypertensive, and glaucoma eyes following acute intraocular pressure elevation. IOVS 57:4869–4877

Wang P, Pierron F, Thomsen OT (2013) Identification of material parameters of PVC foams using digital image correlation and the virtual fields method. Exp Mech 53:1001–1015

Wang X et al (2016) Finite element analysis predicts large optic nerve head strains during horizontal eye movementseye movements induce optic nerve head strains. Investig Ophthalmol Vis Sci 57:2452–2462

Wollensak G, Spoerl E (2004) Collagen crosslinking of human and porcine sclera. J Cataract Refract Surg 30:689–695

Woo SL, Kobayashi aS, Schlegel Wa, Lawrence C (1972) Nonlinear material properties of intact cornea and sclera. Exp Eye Res 14:29–39

Yoon S-h, Giannakopoulos I, Siviour CR (2015) Application of the virtual fields method to the uniaxial behavior of rubbers at medium strain rates. Int J Solids Struct 69:553–568

Zhang L, Albon J, Jones H, Gouget CL, Ethier CR, Goh JC, Girard MJ (2015) Collagen microstructural factors influencing optic nerve head biomechanics. Investig Ophthalmol Vis Sci 56:2031–2042